

# Achieving Ultra-High-Energy-Density Lithium Batteries: Elimination of Irreversible Anionic Redox through Controlled Cationic Disordering

Minjun Wang,<sup>◆</sup> Changming Ke,<sup>◆</sup> Han Zhang, Chuanyu Hou, Juner Chen, Shi Liu,<sup>\*</sup> and Jianhui Wang<sup>\*</sup>



Cite This: *Nano Lett.* 2024, 24, 12343–12352



Read Online

ACCESS |

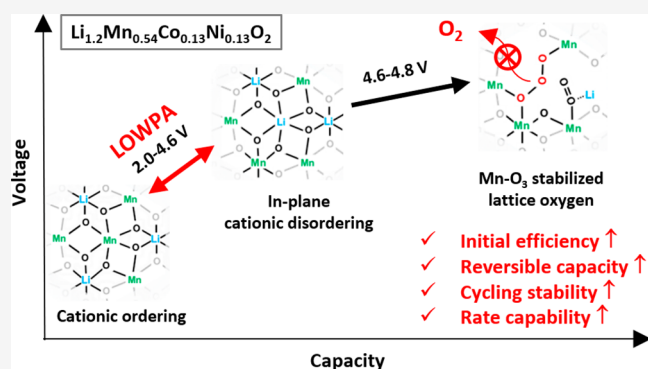
Metrics & More

Article Recommendations

Supporting Information

**ABSTRACT:** Lithium-rich layered oxides (LLOs) capable of supporting both cationic and anionic redox chemistry are promising cathode materials. Yet, their initial charge to high voltages often trigger significant oxygen evolution, resulting in substantial capacity loss and structural instability. In this study, we applied a straightforward low-potential activation (LOWPA) method alongside a relatively stable electrolyte to address this issue. This approach enables precise control over the order-to-disorder transformation of the transition metal layers in LLOs, producing an in-plane cation-disordered  $\text{Li}_{1.2}\text{Mn}_{0.54}\text{Co}_{0.13}\text{Ni}_{0.13}\text{O}_2$  that averts irreversible oxygen evolution at 4.8 V by stabilizing Mn–O<sub>2</sub> or Mn–O<sub>3</sub> species within the Li/Mn-disordered nanopores. Consequently, an ultrahigh reversible capacity of 322 mAh g<sup>-1</sup> (equating to 1141 Wh kg<sup>-1</sup>), 91.5% initial Coulombic efficiency, and enhanced durability and rate capability are simultaneously achieved. As LOWPA does not alter any chemical composition of LLOs, it also offers a simple model for untangling the complex phenomena associated with oxygen-redox chemistry.

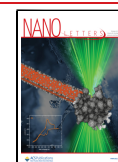
**KEYWORDS:** *Li-rich Mn-based layered oxides, irreversible oxygen evolution, cationic disordering, structural stability, low-potential activation*



For lithium-ion battery technology to address the global challenge of energy storage, the energy density of the battery demands further improvement. Lithium-ion batteries with conventional intercalation cathodes in which the electrochemical driving force relies solely on the cationic redox are reaching their capacity limits.<sup>1,2</sup> Lithium-rich layered oxides (LLOs) have attracted great interest as high-energy-density cathode materials because they can take advantage of both cationic and anionic redox chemistry.<sup>3–6</sup> However, the redox reactions of anions such as lattice oxygen often involve significant irreversible oxygen evolution from the cathode at a high voltage,<sup>7–11</sup> causing intricate and complex issues such as severe structural instabilities,<sup>12–14</sup> large capacity loss,<sup>15–17</sup> poor initial Coulombic efficiency (CE),<sup>9,16,18</sup> and pernicious side reactions between the cathode and electrolyte.<sup>19–22</sup> To date, the simultaneous presence of high reversible capacity, high initial CE and high structural stability remains unattainable for LLOs<sup>11,23–25</sup> This reflects the dilemma of LLO cathodes: the anionic redox chemistry involving lattice oxygen is required to obtain high capacity whereas active lattice oxygen may easily cause irreversible oxygen evolution that is detrimental to the battery performance.

Numerous strategies have been proposed to inhibit irreversible oxygen evolution of LLO cathodes, such as oxygen vacancy injection,<sup>26–28</sup> spinel coating/integration,<sup>29–31</sup> and anion doping.<sup>32–34</sup> The essence of those methods is to reduce the activity of lattice oxygen, which improves the charge–discharge reversibility but inevitably suppresses the oxygen redox, thus sacrificing the energy density.<sup>26–34</sup> In addition, efforts have also been made via regulating the cationic disordering of LLO materials,<sup>35,36</sup> yet they often demand multiple treatments that will increase the manufacturing cost. Nevertheless, a significant amount of irreversible oxygen loss at high voltages is still observed. Although LLO cathodes may deliver a theoretical capacity of ~380 mAh g<sup>-1</sup>, a practical reversible capacity above 300 mAh g<sup>-1</sup> remains challenging.<sup>10,25,37–39</sup> And the initial CEs of most reports are less than

**Received:** March 31, 2024  
**Revised:** September 10, 2024  
**Accepted:** September 11, 2024  
**Published:** September 16, 2024



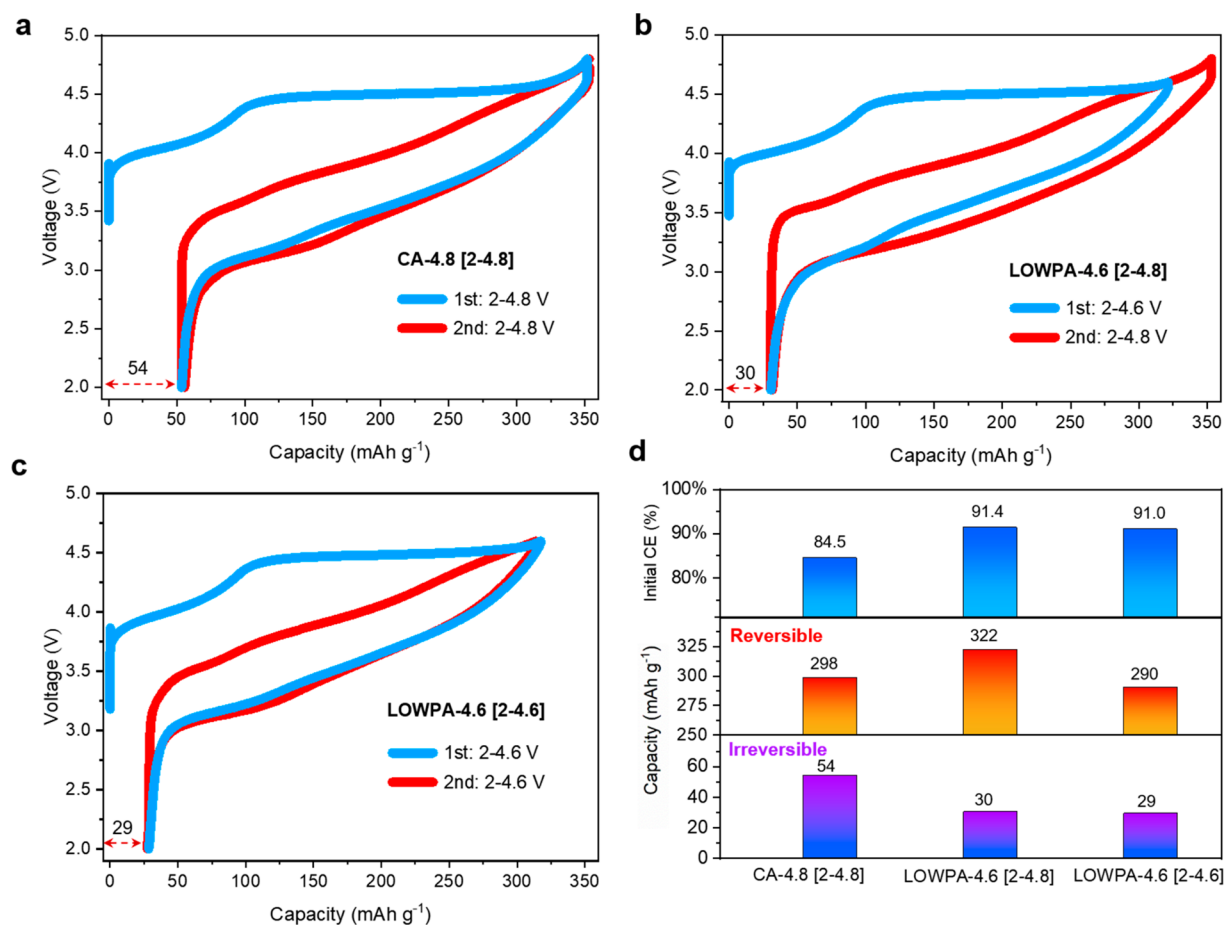


**Figure 1.** Electrochemical performances of  $\text{Li}_{1.2}\text{Mn}_{0.54}\text{Co}_{0.13}\text{Ni}_{0.13}\text{O}_2$  electrodes with different treatments. (a) Conventional activation at 2–4.8 V (CA-4.8) followed by a second cycle at 2–4.8 V, denoted as CA-4.8 [2–4.8]. (b) Low-potential activation at 2–4.6 V (LOWPA-4.6) followed by a second cycle at 2–4.8 V, denoted as LOWPA-4.6 [2–4.8]. (c) Testing LOWPA-4.6 followed by a second cycle at 2–4.6 V, denoted as LOWPA-4.6 [2–4.6]. (d) Comparison of reversible and irreversible capacities and initial CEs treated by different methods. Initial CE = reversible capacity/(reversible + irreversible capacities)  $\times$  100%.

85%,<sup>28,37,39</sup> which is far below the practical requirement of >90%. Therefore, a cost-efficient approach that eliminates irreversible oxygen redox but causes no negative impact on the practical capacity is imperatively demanded to promote the commercialization of LLO cathodes.

The long-standing challenge of oxygen-redox cathodes seems to suggest that there is always a trade-off between structural stability and energy density. In this work, we discover that the evolving structures of LLO cathodes during the first charge–discharge cycling have drastically different stabilities that can be utilized to break the trade-off. By combining a simple low-potential charge–discharge activation (LOWPA) method with a relatively stable electrolyte, the irreversible oxygen redox of LLO cathodes at high voltages is effectively eliminated, and simultaneously an ultrahigh reversible capacity (322  $\text{mAh g}^{-1}$ , corresponding to 1141  $\text{Wh kg}^{-1}$ ), high initial CE (91.5%), and improved cycling stability and rate capability are achieved. A series of characterizations, including operando differential electrochemical mass spectrometry (DEMS) and in situ X-ray powder diffraction (XRD), demonstrate that LOWPA operated within an appropriate voltage window drives a controlled order-to-disorder structural transformation of the transition metal (TM) layers of LLOs during which the lattice oxygen remains stable. The obtained LLOs with disordered TM layers possess

enhanced stability, capable of supporting reversible anionic redox at a high voltage (up to 4.8 V). Such controllable structural disordering of LLOs enabled by LOWPA, involving no chemical compositional change, is simple to implement, which not only boosts the commercialization of LLO-based high-energy-density batteries but also provides an ideal model to disentangle the entangled phenomena associated with oxygen-redox chemistry.

**LOWPA Improves Electrochemical Performances.** The Li-rich layered oxide of  $\text{Li}_{1.2}\text{Mn}_{0.54}\text{Co}_{0.13}\text{Ni}_{0.13}\text{O}_2$  was synthesized by a coprecipitation method without any surface-coating or doping treatment (see the “Experimental” section in the Supporting Information). The obtained powder sample is made of spherical particles with a typical diameter of  $\sim 15 \mu\text{m}$ ; the structure is identified as a well-defined layered configuration with combined  $\text{LiTMO}_2$  ( $R\bar{3}m$ ) and  $\text{Li}_2\text{MnO}_3$  ( $C/2m$ ) phases (see Figure S1). The reversible charge–discharge capacity was tested in a half-cell using a relatively stable electrolyte of 1 M  $\text{LiPF}_6$  + 0.2 M  $\text{LiDFOB}$  in fluorine solvents. Figure 1a displays the initial charge–discharge curve of  $\text{Li}_{1.2}\text{Mn}_{0.54}\text{Co}_{0.13}\text{Ni}_{0.13}\text{O}_2$  over a voltage range of 2–4.8 V at 0.1 C (denoted as conventional activation, CA-4.8). The sloping region (<4.45 V) and plateau region (>4.45 V) correspond to cationic redox (e.g.,  $\text{Ni}^{2+}/\text{Ni}^{4+}$  and  $\text{Co}^{3+}/\text{Co}^{4+}$ ) and oxygen-redox reactions, respectively. The obtained charge

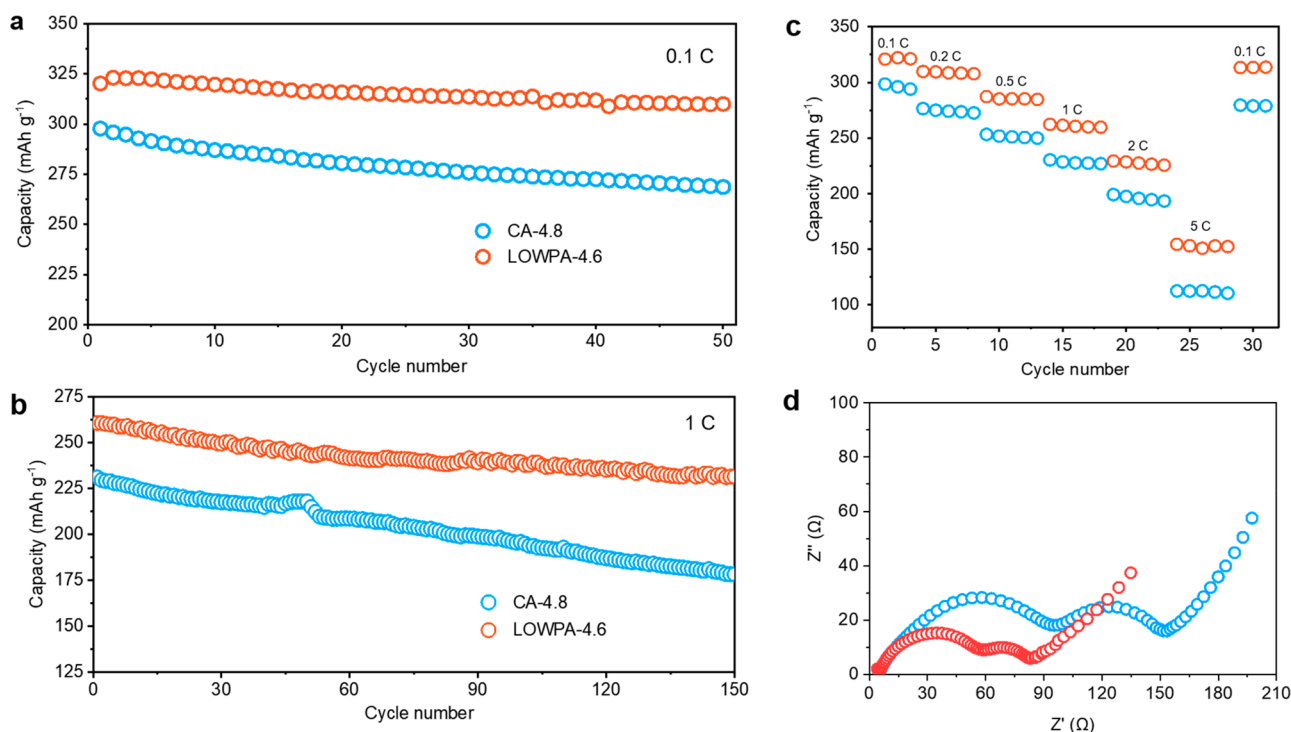


**Figure 2.** Capacity stability and rate performance of  $\text{Li}_{1.2}\text{Mn}_{0.54}\text{Co}_{0.13}\text{Ni}_{0.13}\text{O}_2$  treated by CA-4.8 and LOWPA-4.6. Cycle performances at (a) 0.1 and (b) 1 C. (c) Comparison of rate performances at different current densities. (d) Nyquist plots measured at 4.0 V for  $\text{Li}_{1.2}\text{Mn}_{0.54}\text{Co}_{0.13}\text{Ni}_{0.13}\text{O}_2$  electrodes after CA-4.8 and LOWPA-4.6.

and discharge capacities are  $351.8$  and  $298.2$   $\text{mAh g}^{-1}$ , respectively, resulting in a large irreversible capacity of  $53.6$   $\text{mAh g}^{-1}$  and low initial CE of  $84.7\%$ , which is unacceptable for practical applications. Overall, these results show the typical characteristic of Li-rich Mn-based layered oxides consistent with the literature.<sup>3,5,26,27</sup>

The LOWPA method developed in this work is rather simple: performing a straightforward charge–discharge cycle between 2.0 and 4.6 V, denoted as LOWPA-4.6. Remarkably, after the LOWPA-4.6 treatment, we obtain an ultrahigh discharge capacity of  $321.6$   $\text{mAh g}^{-1}$  (corresponding to  $1141$   $\text{Wh kg}^{-1}$ ) at the subsequent cycling over a voltage window of 2–4.8 V (denoted as LOWPA-4.6 [2–4.8], see Figure 1b). As a comparison, we performed another test by first treating the cell with LOWPA-4.6 and then cycling the cell in a lower voltage region of 2.0–4.6 V (denoted as LOWPA-4.6 [2–4.6], see Figure 1c). The reversible and irreversible capacities using different treatments are summarized in Figure 1d. The nearly identical irreversible capacity ( $\sim 30$   $\text{mAh g}^{-1}$ ) for LOWPA-4.6 [2–4.6] and LOWPA-4.6 [2–4.8] hints that LOWPA-4.6 could make the oxygen redox highly reversible in the high-voltage region of 4.6–4.8 V. Specifically, LOWPA-4.6 increases the capacity reversibility within 4.6–4.8 V from 27% in CA-4.8 to 97% (see Figure S2), indicating an extraordinary effect on reducing irreversible capacity loss during high-voltage anionic redox reactions. With the irreversible capacity being considerably reduced from  $53.6$  to  $30$   $\text{mAh g}^{-1}$  and reversible capacity being increased from  $298.2$  to  $321.6$   $\text{mAh g}^{-1}$ , the overall initial CE is greatly increased to  $91.5\%$  by the LOWPA-4.6 treatment (Figure 1d), beneficial for practical application.

Figure 2 shows the cycling stability and rate capability of  $\text{Li}_{1.2}\text{Mn}_{0.54}\text{Co}_{0.13}\text{Ni}_{0.13}\text{O}_2$  with and without the LOWPA treatment. Clearly, the battery treated by LOWPA-4.6 shows a much better cycling durability than that treated by CA-4.8 at

both 0.1 C ( $96.8$  vs  $90.2\%$  in 50 cycles, see Figure 2a) and 1 C ( $89.2$  vs  $75.1\%$  in 150 cycles, see Figure 2b). Even at high rates of 1, 2, and 5 C, the battery treated by LOWPA-4.6 delivers high capacities of  $262.3$ ,  $230.3$ , and  $155.6$   $\text{mAh g}^{-1}$ , respectively, showing an improved rate capability (Figures 2c and S3). Electrochemical impedance spectroscopy (EIS) measurements reveal that the battery treated by LOWPA exhibits considerably lower resistances of  $\text{Li}^+$ -diffusion at surface layers and charge transfer (Figure 2d), confirming that LOWPA treatment improves the electrode–electrolyte interface. Hence, our simple LOWPA approach accomplishes simultaneously high initial CE ( $91.5\%$ ), high reversible capacity ( $322$   $\text{mAh g}^{-1}$ ), and improved cycling stability and rate capability without using complicated and expensive material treatments, demonstrating significant advantages over other strategies reported previously (see Table S1).

We also tested the LOWPA method using different electrolytes and electrodes. For the electrolyte of 1 M  $\text{LiPF}_6/\text{EC}:\text{DMC}$ , the initial CE and reversible capacity are increased from  $74.3\%$  to  $86.0\%$  and from  $226$  to  $259$   $\text{mAh g}^{-1}$ , respectively; for the electrolyte of 1 M  $\text{LiPF}_6/\text{EC}:\text{DMC}:\text{DEC}$ , the initial CE and reversible capacity are increased from  $84.8\%$  to  $91.1\%$  and from  $263$  to  $286$   $\text{mAh g}^{-1}$ , respectively (see Figure S4). Besides, LOWPA also works on the  $\text{Li}_{1.2}\text{Mn}_{0.6}\text{Ni}_{0.2}\text{O}_2$  and  $\text{Li}_2\text{MnO}_3$  electrodes in both carbonate and fluorine electrolytes (see Figures S5 and S6). Obviously, the LOWPA strategy improves both the initial CE and reversible capacity independent of electrodes and electrolytes, evidencing its universality. Among them, the results on the conventional carbonate electrolytes are consistent with previous reports.<sup>40–42</sup> However, these improvements using the carbonate electrolytes are not as good as that using the fluorine electrolyte, which should be due to less stability of the carbonate electrolytes at high voltages.<sup>3,19–22</sup> Because the

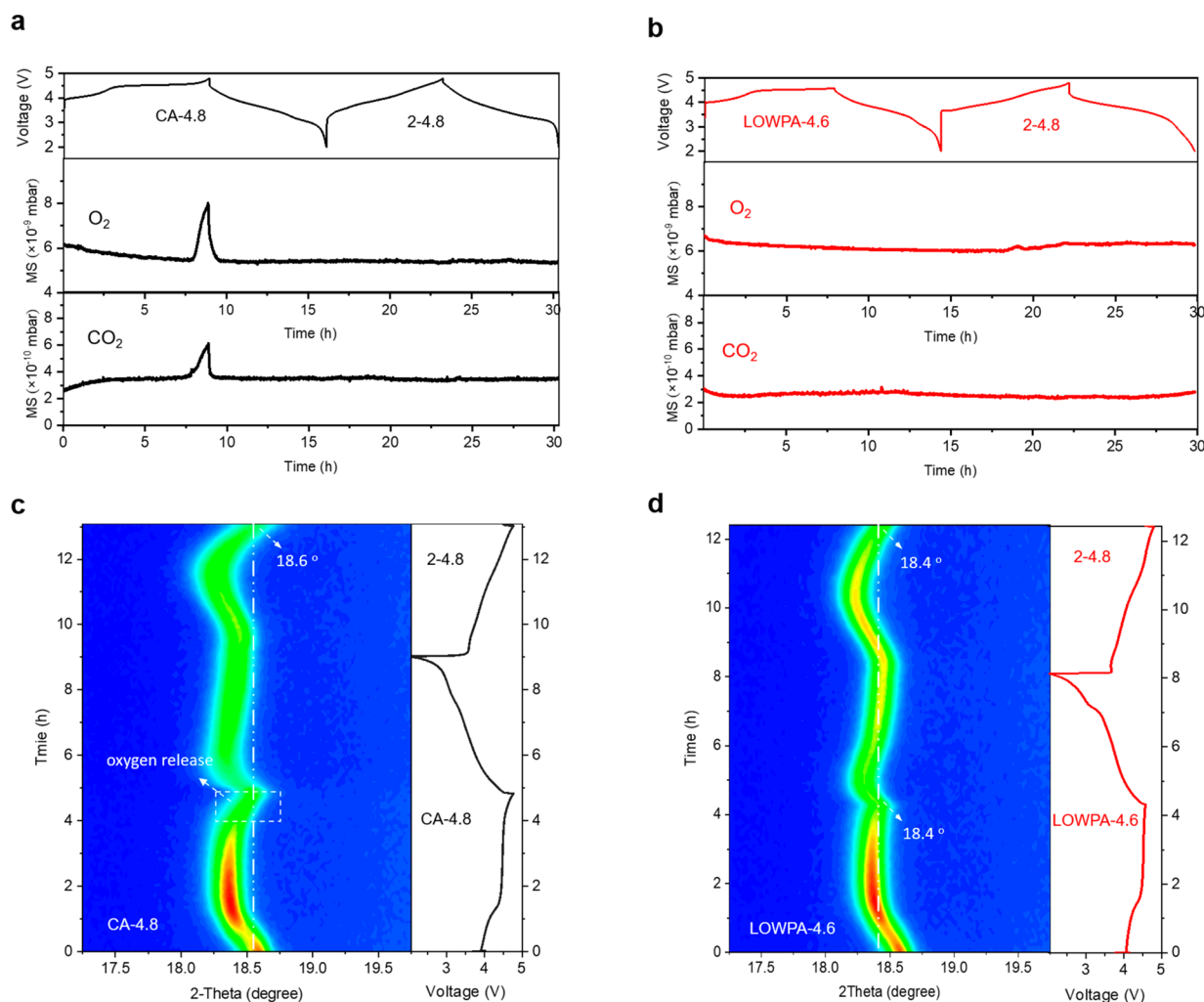


**Figure 3.** Operando DEMS and in situ XRD characterizations of  $\text{Li}_{1.2}\text{Mn}_{0.54}\text{Co}_{0.13}\text{Ni}_{0.13}\text{O}_2$  electrodes with different treatments. (a and c) CA-4.8 followed by second charge/discharge. (b and d) LOWPA-4.6 followed by second charge/discharge. The charge–discharge rates in operando DEMS and in situ XRD measurements are 0.1 and 0.2 C, respectively.

electrolyte instability will inevitably bring additional factors affecting the electrochemical performances, which is not beneficial for disclosing the role of LOWPA, the following investigations focus only on the  $\text{Li}_{1.2}\text{Mn}_{0.54}\text{Co}_{0.13}\text{Ni}_{0.13}\text{O}_2$  electrode using a stable fluorine electrolyte.

**LOWPA Eliminates Irreversible Oxygen Evolution at 4.8 V.** The highly reversible anionic redox chemistry enabled by LOWPA stimulates us to carry out operando DEMS and in situ XRD to detect oxygen evolution under different treatments. Figure 3a shows the evolution of  $\text{O}_2$  during the CA-4.8 treatment followed by a second cycle between 2 and 4.8 V. During the first charge, no  $\text{O}_2$  is detected before 4.6 V, while a substantial amount of  $\text{O}_2$  and  $\text{CO}_2$  is produced when the voltage is above 4.6 V; during the second 2–4.8 V charge, no significant release of  $\text{O}_2$  and  $\text{CO}_2$  release occurs. These results reveal that the irreversible anionic redox reactions that lead to  $\text{O}_2$  release and the oxidation of electrolyte predominantly occurs at a high voltage above 4.6 V in the first charge, and the lattice oxygen becomes more stable after the first charge–discharge cycle, consistent with the previous reports.<sup>3,43–46</sup> The evolution of the  $\text{O}_2$  during the LOWPA-4.6 treatment (a full charge–discharge cycle over 2–4.6 V) followed by a second cycle between 2 and 4.8 V is shown in Figure 3b. Notably, no significant  $\text{O}_2$  and  $\text{CO}_2$  can be detected

during the whole process, indicating an elimination of irreversible anionic redox reactions even in the high-voltage region of 4.6–4.8 V. The drastically different  $\text{O}_2$  evolutions under different treatments are corroborated by in situ XRD measurements that track the (003) reflection peak of the  $\text{Li}_{1.2}\text{Mn}_{0.54}\text{Co}_{0.13}\text{Ni}_{0.13}\text{O}_2$ . For the CA-4.8 treatment (Figures 3c and S7), the (003) reflection peak notably shifts from  $18.4^\circ$  to  $18.6^\circ$  (corresponding to a decrease of the unit cell size) when first charged from 4.6 to 4.8 V, which is a typical feature of  $\text{O}_2$  release.<sup>29,30</sup> By contrast, after the LOWPA-4.6 treatment, the (003) reflection peak remains at a small angle of  $18.4^\circ$  when it is first charged to 4.8 V, which is the same as that when it is first charged to 4.6 V during LOWPA-4.6 (Figures 3d and S7), substantiating the DEMS results that show no sign of  $\text{O}_2$  release. Therefore, combining the operando DEMS and in situ XRD investigations, we firmly evidence that LOWPA-4.6 can eliminate  $\text{O}_2$  release up to 4.8 V.

**LOWPA Induces Cationic Disorder and Enhanced Stability.** To understand why LOWPA eliminates the release of the  $\text{O}_2$  at high voltages, we studied the change of the material structure and stability under different treatments. Figures 4a and S8 demonstrate the XRD patterns of  $\text{Li}_{1.2}\text{Mn}_{0.54}\text{Co}_{0.13}\text{Ni}_{0.13}\text{O}_2$  electrodes before and after LOWPA treatment. Both patterns look identical except the characteristic

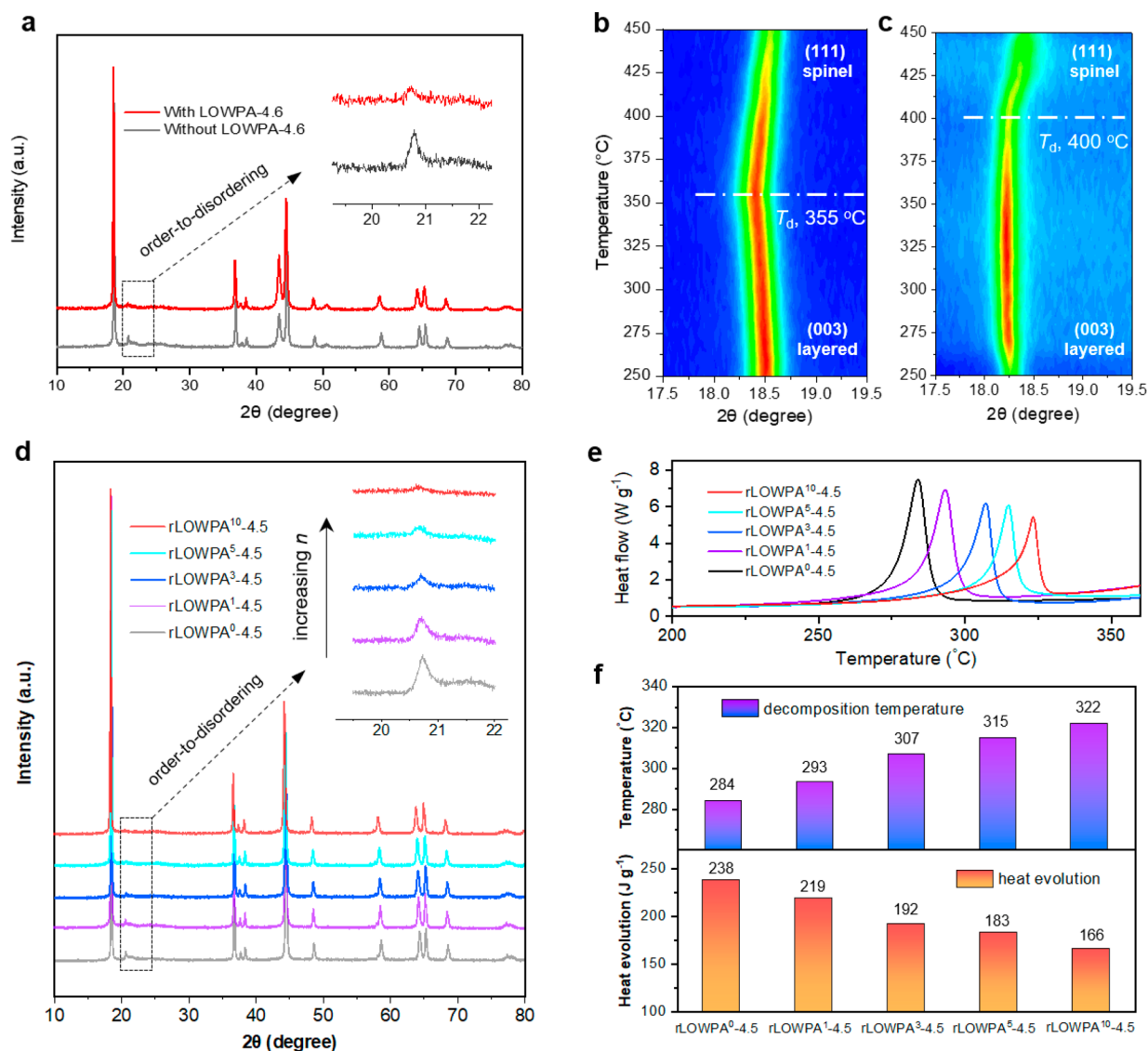


**Figure 4.** Cationic disordering driven by LOWPA and its impact on structural stability. (a) XRD characterizations of  $\text{Li}_{1.2}\text{Mn}_{0.54}\text{Co}_{0.13}\text{Ni}_{0.13}\text{O}_2$  electrodes with and without LOWPA-4.6. (b and c) In situ variable-temperature XRD characterizations of  $\text{Li}_{1.2}\text{Mn}_{0.54}\text{Co}_{0.13}\text{Ni}_{0.13}\text{O}_2$  electrodes at the full charge state of 4.8 V without and with LOWPA-4.6, respectively. (d) XRD characterizations of  $\text{Li}_{1.2}\text{Mn}_{0.54}\text{Co}_{0.13}\text{Ni}_{0.13}\text{O}_2$  electrodes treated by  $\text{rLOWPA}^n\text{-4.5}$  ( $n = 0$  means the electrode is without treatment). The inset shows the gradual disappearance of the  $\text{LiMn}_6$  honeycomb superlattice with the increase of cycle number of LOWPA-4.5 treatment, demonstrating the delicate control of the order-to-disorder transformation in the TM layer of LLO. (e) DSC characterizations of electrodes at a charge state of 4.6 V after the treatment of  $\text{rLOWPA}^n\text{-4.5}$  with the corresponding heat evolution summarized in (f). The charged and discharged capacities of the DSC samples are listed in Table S3.

peak at 20–23° (corresponding to the  $\text{LiMn}_6$  honeycomb superlattice of the LLOs) becomes substantially suppressed after LOWPA, indicating the generation of an in-plane cationic-disordered structure during the LOWPA treatment.<sup>47–51</sup> On the other hand, the stability of the  $\text{Li}_{1.2}\text{Mn}_{0.54}\text{Co}_{0.13}\text{Ni}_{0.13}\text{O}_2$  electrodes obtained at 4.8 V with and without LOWPA treatment was evaluated by in situ variable-temperature XRD measurements. Generally, the (003) peak shifts toward lower angles with increasing temperatures but undergoes a sharp shift to larger angles at a decomposition temperature ( $T_d$ ), accompanied by the emergence of new reflection peaks corresponding to the (111) plane of the spinel structure.<sup>30</sup> The value of  $T_d$  is thus a direct gauge of the cathode stability. After the LOWPA-4.6 treatment, the resulting material has a  $T_d$  of 400 °C, higher than the value of  $T_d$  of 355 °C for that directly charged to 4.8 V (see Figures

4b and 4c), indicating that LOWPA effectively enhances the stability of  $\text{Li}_{1.2}\text{Mn}_{0.54}\text{Co}_{0.13}\text{Ni}_{0.13}\text{O}_2$ . Therefore, it is likely that LOWPA induces an in-plane cationic-disordered structure with enhanced stability.

As is well-known, an irreversible loss of in-plane cationic ordering of the TM layer together with a significant amount of  $\text{O}_2$  release is generally observed in the Li-rich Mn-based oxides at a conventional activation to 4.8 V.<sup>47–51</sup> The different  $\text{O}_2$  evolution between LOWPA-4.6 and CA-4.8 could be resulted from different degrees of the in-plane cationic disordering; the former induces a higher degree of cationic disordering which can stabilize the material without  $\text{O}_2$  evolution at high voltages while the latter cannot induce sufficient cationic disordering so that the material is not stable enough to suppress the  $\text{O}_2$  evolution at high voltages. Based on the assumption, a low-potential charge–discharge activation is required to induce

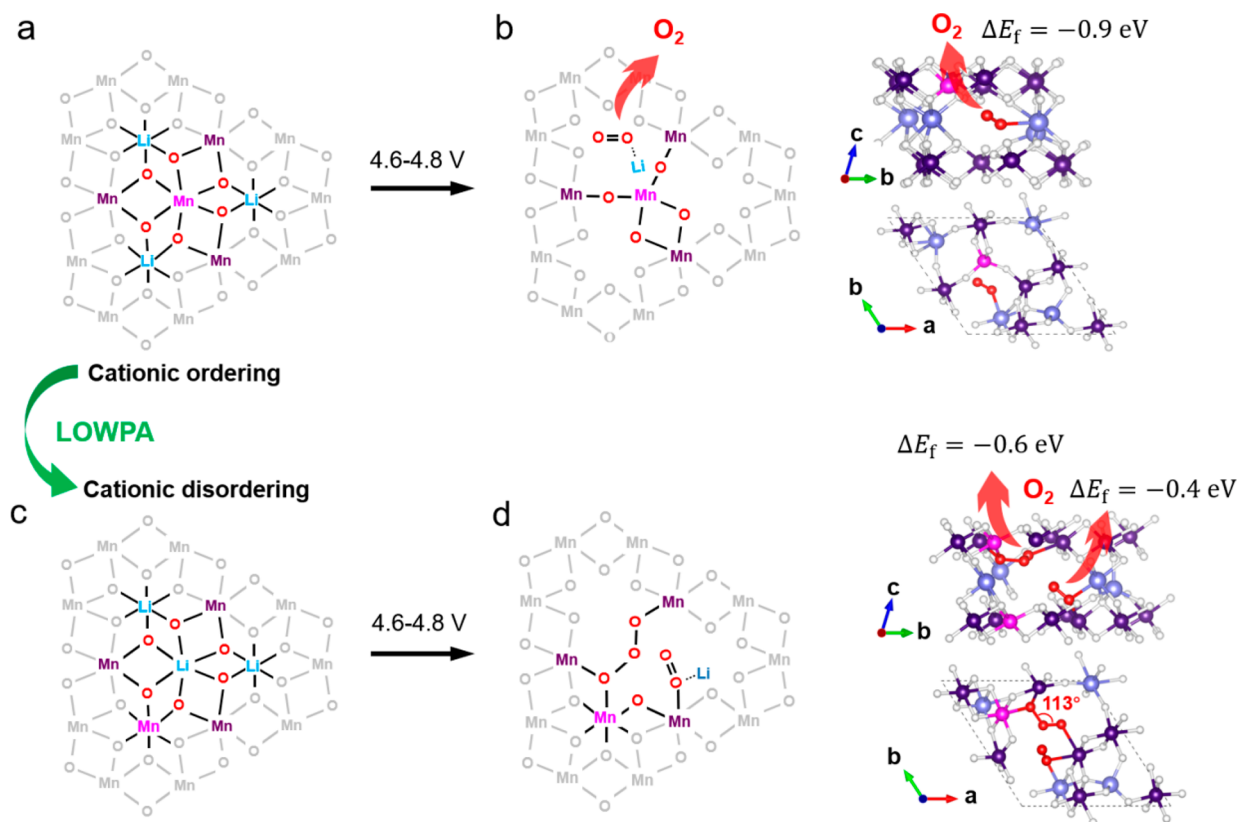


**Figure 5.** Mechanism of LOWPA. (a) Schematics of as-prepared  $\text{Li}_2\text{MnO}_3$  cathodes with ordered transition metal layers. (b) Oxygen loss when charged to a high voltage due to a low oxygen formation energy,  $\Delta E_f = E_{\text{Li}_4\text{Mn}_8\text{O}_{22}} + E_{\text{O}_2} - E_{\text{Li}_4\text{Mn}_8\text{O}_{24}}$ . (c) Schematics of  $\text{Li}_2\text{MnO}_3$  with disordered transition metal layers after LOWPA. (d) Delithiated configuration with Mn coordinated with six oxygen atoms and the formation of  $\text{Mn-O}_2$  or  $\text{Mn-O}_3$  species stabilized in the Li/Mn-disordered nanopores. The oxygen formation energy becomes higher, supporting the suppression of irreversible oxygen evolution in the in-plane Li/Mn disordered  $\text{Li}_2\text{MnO}_3$ . The O–O–O angle of  $113^\circ$  shows a typical characteristic for an ozonic ion ( $\text{O}_3^-$ ).

sufficient in-plane cationic disordering before operation at high voltages where the irreversible  $\text{O}_2$  release occurs.

To validate the assumption above, we introduce repeated LOWPA, that is, performing LOWPA at a relatively low potential for multiple cycles ( $n$ ), denoted as rLOWPA<sup>*n*</sup>, by which the in-plane cationic order-to-disorder change can be observed in more detail. As shown in Figures 4d and S9, at a lower activation potential of 4.5 V, the rLOWPA<sup>*n*</sup>-4.5 induces a gradual disappearance of the superlattice peak ( $\sim 21^\circ$ ) together with a gradual shortening of the oxygen-redox voltage plateau in the 4.45–4.6 V region as  $n$  increases from 0 to 10, demonstrating the progressive disordering of  $\text{Li}^+$  and  $\text{Mn}^{4+}$  in TM layers driven by the repeated LOWPA. Interestingly, a widening low-voltage plateau appears at 2.9–3.2 V after rLOWPA<sup>*n*</sup>-4.5 treatment, which is due to the oxygen-redox reactions rather than the formation of the spinel phase (see discussion in Figure S10). Besides, the (003)/(104) diffraction ratios are all higher than 2.3 during the whole process of rLOWPA<sup>*n*</sup>-4.5 ( $n = 0-10$ ), reflecting that the interlayer disordering during the LOWPA treatment is negligible<sup>52,53</sup> (see Table S2). Similar features are presented in the Raman spectra, as shown in Figure S11. On the other hand, a gradual enhanced stability of  $\text{Li}_{1.2}\text{Mn}_{0.54}\text{Co}_{0.13}\text{Ni}_{0.13}\text{O}_2$  during the process of rLOWPA<sup>*n*</sup>-4.5 was indeed detected by differential scanning calorimetry (DSC, see Figures 4e and 4f), which thus firmly confirms the correlation between the cathode stability and the degree of structural disordering in TM layers. The

enhanced stability of  $\text{Li}_{1.2}\text{Mn}_{0.54}\text{Co}_{0.13}\text{Ni}_{0.13}\text{O}_2$  could eliminate the  $\text{O}_2$  evolution at high voltages, leading to an improved initial CE and reversible capacity (see Figure 1); meanwhile, this also facilitates to stabilize the electrode/electrolyte interphase, contributing to an improved rate capability and cycling durability (see Figure 2). In addition, we also tried different activation potentials and found that a too low activation potential ( $<4.4 \text{ V}$ ) does not work (see Figures S12 and S13). Thus, a suitable activation potential, which is higher than the onset potential of oxygen redox but lower than that of irreversible oxygen evolution, is required for LOWPA. In the case of  $\text{Li}_{1.2}\text{Mn}_{0.54}\text{Co}_{0.13}\text{Ni}_{0.13}\text{O}_2$ , the suitable activation potential for LOWPA is between 4.45 and 4.6 V.

**Mechanistic Understanding of LOWPA Effects.** Based on our detailed experimental characterizations, we propose a working mechanism of LOWPA as illustrated in Figure 5 with supporting evidence from first-principles density functional theory (DFT) calculations. We first note that when the  $\text{Li}_{1.2}\text{Mn}_{0.54}\text{Co}_{0.13}\text{Ni}_{0.13}\text{O}_2$  electrode (Figure 5a) is first charged to 4.8 V, the TM layers cannot fully convert into the disordered state (Figure 5b), and the lattice oxygen in the delithiated configuration with partial ordering forms a  $\text{O}_2$ -Li species, which may easily induce  $\text{O}_2$  release,<sup>3,7,9,54</sup> thus deteriorating the structural integrity and causing capacity loss in subsequent cycles. This is consistent with a negative  $\text{O}_2$ -formation energy of  $-0.9 \text{ eV}$  for delithiated  $\text{Li}_2\text{MnO}_3$  ( $\text{Li}_4\text{Mn}_8\text{O}_{24}$ ) calculated by DFT. In comparison, the activation

potential in LOWPA (4.45–4.6 V) is high enough to drive Li ions diffusing out of TM layers, which helps TM migration, but not too high to activate the irreversible oxygen evolution reaction. Our DFT investigations show that the Li ion diffusion facilitates the migration of TM ions to vacant sites with six coordinated oxygen atoms (see Figure S14). After the LOWPA treatment, the electrode possesses highly disordered TM layers (Figure 5c). We found two  $O_2^{2-}$ -derived motifs stabilized in the TM-disordered nanopores. One  $O_2^{2-}$  is bonded to Li and Mn with a formation energy of  $-0.4$  eV. Another  $O_2^{2-}$  acts as a bridge between Mn and O ions and forms a stable structure during delithiation, leading to an ozonic ion ( $O_3^-$ , featured with an O–O–O angle of  $113^\circ$ ) (see Figures 5d, S15, and S16). This structure has a higher  $O_2$ -formation energy of  $-0.6$  eV than the TM-ordered structures, explaining the elimination of the  $O_2$  release. It is noted that some ozonides such as  $N(CH_3)_4O_3$  have been synthesized and could be stable at room temperature.<sup>55</sup> Therefore, LOWPA essentially creates, in an  $O_2$ -release-free manner, disordered TM layers that exhibit a high  $O_2$ -evolution potential, consequently supporting reversible anionic redox over a high voltage window (e.g., 4.6–4.8 V) without  $O_2$  release. Additionally, the disordering process can be well controlled via rLOWPA<sup>n</sup> by varying the potential magnitude and the cycling number.

Previously, LLO cathodes, though they present a prominent advantage of high capacity, often suffer from a fast decay of energy density due to various entangled issues, such as cationic order-to-disorder transformation, layer-to-spinel phase change, oxygen loss, voltage decline, and interphase deterioration.<sup>12–18</sup> The coexistence of reversible oxygen redox and irreversible oxygen evolution in LLO makes it difficult to clarify the origin of the entangled phenomena. Our work successfully eliminates the irreversible oxygen evolution at high voltages by a simple LOWPA method without chemical compositional change, providing a good model to revisit the key issue associated with oxygen-redox chemistry. Combining experimental and theoretical results, it clearly indicates that the LLO cathode with a highly disordered TM layer has a higher stability, which supports reversible oxygen redox at high voltages without oxygen loss and achieves a high initial CE and reversible capacity as well as improved cycling durability. The enhanced stability of the in-plane TM-disordered structure is the driving force that induces the cationic order-to-disorder transformation generally observed in the initial activation process of LLO. On the other hand, the LOWPA-treated sample still undergoes a significant voltage decline and layer-to-spinel phase change (see Figure S17), which indicates that the irreversible oxygen evolution is not primarily responsible for either the voltage decline or the layer-to-spinel phase change during the charge–discharge cycling. Further in-depth study is required to clarify the mechanism in the future.

In summary, we demonstrate a simple yet effective LOWPA method to control the in-plane cationic disordering of LLOs with the help of a stable electrolyte, potentially overcoming the generally observed trade-off between the energy density and structural stability of LLOs. An ultrahigh reversible capacity ( $322 \text{ mAh g}^{-1}$ , corresponding to  $1141 \text{ Wh kg}^{-1}$ ) with high initial CE (91.5%) and improved cycling durability and rate capability are simultaneously achieved on the  $Li_{1.2}Mn_{0.54}Co_{0.13}Ni_{0.13}O_2$  cathode. A series of experiments including operando DEMS and in situ XRD measurements establish the correlation between the disordering degree of TM layers and the evolving structural stability of LLOs during

charge–discharge cycles, by which it unravels a clear rule: that is, the higher degree of in-plane cationic disordering, the higher stability of the LLO material, and the lower irreversible oxygen release at high voltages. This finding is different from the conventional view that usually regards the cationic disordering in the initial activation process as an unfavorable change responsible for large voltage hysteresis and energy loss. The LOWPA method is operated at an appropriate voltage that should be higher than the onset potential of oxygen redox but lower than that of irreversible oxygen evolution (4.45–4.6 V for the  $Li_{1.2}Mn_{0.54}Co_{0.13}Ni_{0.13}O_2$  material); it drives a controlled disordering of TM layers in an  $O_2$ -release-free manner, leading to a new configuration of LLOs that exhibits a high  $O_2$ -evolution potential beyond 4.8 V due to the formation of Mn– $O_2$  or Mn– $O_3$  species stabilized in the Li/Mn-disordered nanopores. These findings of our study not only provide a simple and effective method to eliminate irreversible anion redox for the development of high-energy-density lithium-ion batteries but also disentangle the entangled phenomena associated with oxygen-redox chemistry. It explains why there is always a cationic order-to-disorder transformation in the initial activation process and clarifies that the irreversible oxygen evolution is not primarily responsible for either the voltage decline or layer-to-spinel phase change during the subsequent charge–discharge cycling. These new insights shed light on approaches to further improve the high-energy-density LLO cathodes.

## ■ ASSOCIATED CONTENT

### SI Supporting Information

The Supporting Information is available free of charge at <https://pubs.acs.org/doi/10.1021/acs.nanolett.4c01532>.

Experimental section summarizing material preparation, characterizations, electrochemical measurements, and computation details (PDF)

## ■ AUTHOR INFORMATION

### Corresponding Authors

Shi Liu – Research Center for Industries of the Future and Department of Physics, School of Science, Westlake University, Hangzhou 310030, China; Institute of Natural Sciences, Westlake Institute for Advanced Study, Hangzhou 310024, China; [orcid.org/0000-0002-8488-4848](https://orcid.org/0000-0002-8488-4848); Email: [liushi@westlake.edu.cn](mailto:liushi@westlake.edu.cn)

Jianhui Wang – Research Center for Industries of the Future and Zhejiang Key Laboratory of 3D Micro/Nano Fabrication and Characterization, School of Engineering, Westlake University, Hangzhou 310030, China; Institute of Advanced Technology, Westlake Institute for Advanced Study, Hangzhou 310024, China; Division of Solar Energy Conversion and Catalysis at Westlake University, Zhejiang Baima Lake Laboratory Co., Ltd., Hangzhou 310000, China; [orcid.org/0000-0002-4170-1132](https://orcid.org/0000-0002-4170-1132); Email: [wangjianhui@westlake.edu.cn](mailto:wangjianhui@westlake.edu.cn)

### Authors

Minjun Wang – Institute of Zhejiang University-Quzhou, Quzhou 324000, China; Zhejiang Key Laboratory of 3D Micro/Nano Fabrication and Characterization, School of Engineering, Westlake University, Hangzhou 310030, China; Institute of Advanced Technology, Westlake Institute for Advanced Study, Hangzhou 310024, China

**Changming Ke** – Department of Physics, School of Science, Westlake University, Hangzhou 310030, China; Institute of Natural Sciences, Westlake Institute for Advanced Study, Hangzhou 310024, China

**Han Zhang** – Zhejiang Key Laboratory of 3D Micro/Nano Fabrication and Characterization, School of Engineering, Westlake University, Hangzhou 310030, China; Institute of Advanced Technology, Westlake Institute for Advanced Study, Hangzhou 310024, China

**Chuan-yu Hou** – Zhejiang Key Laboratory of 3D Micro/Nano Fabrication and Characterization, School of Engineering, Westlake University, Hangzhou 310030, China; Institute of Advanced Technology, Westlake Institute for Advanced Study, Hangzhou 310024, China

**Juner Chen** – Zhejiang Key Laboratory of 3D Micro/Nano Fabrication and Characterization, School of Engineering, Westlake University, Hangzhou 310030, China; Institute of Advanced Technology, Westlake Institute for Advanced Study, Hangzhou 310024, China

Complete contact information is available at:

<https://pubs.acs.org/10.1021/acs.nanolett.4c01532>

### Author Contributions

◆ J.W. and M.W. designed the experiments. M.W., H.Z., and C.H. carried out the experiments. S.L. directed the computation. S.L. and C.K. designed and performed the DFT calculations. All authors contributed to the discussion and the manuscript preparation. M.W. and C.K. contributed equally to this work. J.W. conceived and led the project.

### Notes

The authors declare the following competing financial interest(s): J.W. and M.W. are the inventors of a published Chinese patent (CN202111116469.8).

### ACKNOWLEDGMENTS

This work was supported by the Research Center for Industries of the Future, the National Natural Science Foundation of China (Grant 21975207), the China Postdoctoral Science Foundation (Grant 2020M671811), the Westlake Education Foundation, and Zhejiang Baima Lake Laboratory Co., Ltd. The authors thank Prof. Bingwen Hu (from East China Normal University) for his valuable discussion and Dr. Xiaohe Miao (from Westlake Instrumentation and Service Center for Physical Sciences) for her help on the in situ XRD measurements. The computational resource is provided by Westlake HPC Center.

### REFERENCES

- (1) Armand, M.; Tarascon, J.-M. Building better batteries. *Nature* **2008**, *451* (7179), 652–657.
- (2) Whittingham, M. S. Ultimate limits to intercalation reactions for lithium batteries. *Chem. Rev.* **2014**, *114* (23), 11414–11443.
- (3) Luo, K.; Roberts, M. R.; Hao, R.; Guerrini, N.; Pickup, D. M.; Liu, Y. S.; Edstrom, K.; Guo, J.; Chadwick, A. V.; Duda, L. C.; Bruce, P. G. Charge-compensation in 3d-transition-metal-oxide intercalation cathodes through the generation of localized electron holes on oxygen. *Nat. Chem.* **2016**, *8* (7), 684–691.
- (4) Seo, D. H.; Lee, J.; Urban, A.; Malik, R.; Kang, S.; Ceder, G. The structural and chemical origin of the oxygen redox activity in layered and cation-disordered Li-excess cathode materials. *Nat. Chem.* **2016**, *8* (7), 692–697.
- (5) Liu, S.; Liu, Z.; Shen, X.; Li, W.; Gao, Y.; Banis, M. N.; Li, M.; Chen, K.; Zhu, L.; Yu, R.; Wang, Z.; Sun, X.; Lu, G.; Kong, Q.; Bai,

X.; Chen, L. Surface Doping to Enhance Structural Integrity and Performance of Li-Rich Layered Oxide. *Adv. Energy Mater.* **2018**, *8* (31), 1802105.

(6) Guo, W.; Zhang, C.; Zhang, Y.; Lin, L.; He, W.; Xie, Q.; Sa, B.; Wang, L.; Peng, D. A Universal Strategy toward the Precise Regulation of Initial Coulombic Efficiency of Li-Rich Mn-Based Cathode Materials. *Adv. Mater.* **2021**, *33* (38), No. 2103173.

(7) Liu, S.; Wang, B.; Zhang, X.; Zhao, S.; Zhang, Z.; Yu, H. Reviving the lithium-manganese-based layered oxide cathodes for lithium-ion batteries. *Matter* **2021**, *4* (5), 1511–1527.

(8) Koga, H.; Croguennec, L.; Ménétrier, M.; Douhil, K.; Belin, S.; Bourgeois, L.; Suard, E.; Weill, F.; Delmas, C. Reversible Oxygen Participation to the Redox Processes Revealed for  $\text{Li}_{1.20}\text{Mn}_{0.54}\text{Co}_{0.13}\text{Ni}_{0.13}\text{O}_2$ . *J. Electrochem. Soc.* **2013**, *160* (6), A786–A792.

(9) Li, X.; Qiao, Y.; Guo, S.; Xu, Z.; Zhu, H.; Zhang, X.; Yuan, Y.; He, P.; Ishida, M.; Zhou, H. Direct Visualization of the Reversible  $\text{O}^{2-}/\text{O}^-$  Redox Process in Li-Rich Cathode Materials. *Adv. Mater.* **2018**, *30* (14), No. e1705197.

(10) Zuo, W.; Luo, M.; Liu, X.; Wu, J.; Liu, H.; Li, J.; Winter, M.; Fu, R.; Yang, W.; Yang, Y. Li-rich cathodes for rechargeable Li-based batteries: reaction mechanisms and advanced characterization techniques. *Energy Environ. Sci.* **2020**, *13* (12), 4450–4497.

(11) Zhang, H.; Liu, H.; Piper, L. F. J.; Whittingham, M. S.; Zhou, G. Oxygen Loss in Layered Oxide Cathodes for Li-Ion Batteries: Mechanisms, Effects, and Mitigation. *Chem. Rev.* **2022**, *122* (6), 5641–5681.

(12) Fell, C. R.; Qian, D.; Carroll, K. J.; Chi, M.; Jones, J. L.; Meng, Y. S. Correlation Between Oxygen Vacancy, Microstrain, and Cation Distribution in Lithium-Excess Layered Oxides During the First Electrochemical Cycle. *Chem. Mater.* **2013**, *25* (9), 1621–1629.

(13) Lee, S.; Jin, W.; Kim, S. H.; Joo, S. H.; Nam, G.; Oh, P.; Kim, Y.-K.; Kwak, S. K.; Cho, J. Oxygen Vacancy Diffusion and Condensation in Lithium-Ion Battery Cathode Materials. *Angew. Chem., Int. Ed.* **2019**, *58* (31), 10478–10485.

(14) Grenier, A.; Kamm, G. E.; Li, Y.; Chung, H.; Meng, Y. S.; Chapman, K. W. Nanostructure Transformation as a Signature of Oxygen Redox in Li-Rich 3d and 4d Cathodes. *J. Am. Chem. Soc.* **2021**, *143* (15), 5763–5770.

(15) Johnson, C. S.; Kim, J. S.; Lefief, C.; Li, N.; Vaughey, J. T.; Thackeray, M. M. The significance of the  $\text{Li}_2\text{MnO}_3$  component in ‘composite’  $x\text{Li}_2\text{MnO}_3 \cdot (1-x)\text{LiMn}_{0.5}\text{Ni}_{0.5}\text{O}_2$  electrodes. *Electrochem. Commun.* **2004**, *6* (10), 1085–1091.

(16) Thackeray, M. M.; Johnson, C. S.; Vaughey, J. T.; Li, N.; Hackney, S. A. Advances in manganese-oxide ‘composite’ electrodes for lithium-ion batteries. *J. Mater. Chem.* **2005**, *15* (23), 2257–2267.

(17) Shunmugasundaram, R.; Senthil Arumugam, R.; Dahn, J. R. High Capacity Li-Rich Positive Electrode Materials with Reduced First-Cycle Irreversible Capacity Loss. *Chem. Mater.* **2015**, *27* (3), 757–767.

(18) Freire, M.; Kosova, N. V.; Jordy, C.; Chateigner, D.; Lebedev, O. I.; Maignan, A.; Pralong, V. A new active Li-Mn-O compound for high energy density Li-ion batteries. *Nat. Mater.* **2016**, *15* (2), 173–177.

(19) Yabuuchi, N.; Yoshii, K.; Myung, S. T.; Nakai, I.; Komaba, S. Detailed studies of a high-capacity electrode material for rechargeable batteries,  $\text{Li}_2\text{MnO}_3\text{-LiCo}_{1/3}\text{Ni}_{1/3}\text{Mn}_{1/3}\text{O}_2$ . *J. Am. Chem. Soc.* **2011**, *133* (12), 4404–4419.

(20) Freunberger, S. A.; Chen, Y.; Peng, Z.; Griffin, J. M.; Hardwick, L. J.; Barde, F.; Novak, P.; Bruce, P. G. Reactions in the rechargeable lithium- $\text{O}_2$  battery with alkyl carbonate electrolytes. *J. Am. Chem. Soc.* **2011**, *133* (20), 8040–8047.

(21) Piao, J.; Gu, L.; Wei, Z.; Ma, J.; Wu, J.; Yang, W.; Gong, Y.; Sun, Y.; Duan, S.; Tao, X.; Bin, D.; Cao, A.; Wan, L. Phase Control on Surface for the Stabilization of High Energy Cathode Materials of Lithium Ion Batteries. *J. Am. Chem. Soc.* **2019**, *141* (12), 4900–4907.

(22) Grimaud, A.; Demortière, A.; Saubanère, M.; Dachraoui, W.; Duchamp, M.; Doublet, M.-L.; Tarascon, J.-M. Activation of Surface

oxygen sites on an iridium-based model catalyst for the oxygen evolution reaction. *Nat. Energy* **2017**, *2*, No. 16189.

(23) Perez, A. J.; Jacquet, Q.; Batuk, D.; Iadecola, A.; Saubanère, M.; Rousse, G.; Larcher, D.; Vezin, H.; Doublet, M.-L.; Tarascon, J.-M. Approaching the limits of cationic and anionic electrochemical activity with the Li-rich layered rocksalt  $\text{Li}_3\text{IrO}_4$ . *Nat. Energy* **2017**, *2* (12), 954–962.

(24) Ben Yahia, M.; Vergnet, J.; Saubanere, M.; Doublet, M. L. Unified picture of anionic redox in Li/Na-ion batteries. *Nat. Mater.* **2019**, *18* (5), 496–502.

(25) He, W.; Guo, W.; Wu, H.; Lin, L.; Liu, Q.; Han, X.; Xie, Q.; Liu, P.; Zheng, H.; Wang, L.; Yu, X.; Peng, D. Challenges and Recent Advances in High Capacity Li-Rich Cathode Materials for High Energy Density Lithium-Ion Batteries. *Adv. Mater.* **2021**, *33* (50), No. e2005937.

(26) Qiu, B.; Zhang, M.; Wu, L.; Wang, J.; Xia, Y.; Qian, D.; Liu, H.; Hy, S.; Chen, Y.; An, K.; Zhu, Y.; Liu, Z.; Meng, Y. Gas-solid interfacial modification of oxygen activity in layered oxide cathodes for lithium-ion batteries. *Nat. Commun.* **2016**, *7*, 12108.

(27) Zhu, Z.; Yu, D.; Yang, Y.; Su, C.; Huang, Y.; Dong, Y.; Waluyo, I.; Wang, B.; Hunt, A.; Yao, X.; Lee, J.; Xue, W.; Li, J. Gradient Li-rich oxide cathode particles immunized against oxygen release by a molten salt treatment. *Nat. Energy* **2019**, *4* (12), 1049–1058.

(28) Li, Q.; Ning, D.; Wong, D.; An, K.; Tang, Y.; Zhou, D.; Schuck, G.; Chen, Z.; Zhang, N.; Liu, X. Improving the oxygen redox reversibility of Li-rich battery cathode materials via Coulombic repulsive interactions strategy. *Nat. Commun.* **2022**, *13* (1), 1123.

(29) Zhang, X. D.; Shi, J. L.; Liang, J. Y.; Yin, Y. X.; Zhang, J. N.; Yu, X. Q.; Guo, Y. G. Suppressing Surface Lattice Oxygen Release of Li-Rich Cathode Materials via Heterostructured Spinel  $\text{Li}_4\text{Mn}_5\text{O}_{12}$  Coating. *Adv. Mater.* **2018**, *30* (29), 1801751.

(30) Zhang, W.; Sun, Y.; Deng, H.; Ma, J.; Zeng, Y.; Zhu, Z.; Lv, Z.; Xia, H.; Ge, X.; Cao, S.; Xiao, Y.; Xi, S.; Du, Y.; Cao, A.; Chen, X. Dielectric Polarization in Inverse Spinel-Structured  $\text{Mg}_2\text{TiO}_4$  Coating to Suppress Oxygen Evolution of Li-Rich Cathode Materials. *Adv. Mater.* **2020**, *32* (19), 2000496.

(31) Zhu, Z.; Gao, R.; Waluyo, I.; Dong, Y.; Hunt, A.; Lee, J.; Li, J. Stabilized Co-Free Li-Rich Oxide Cathode Particles with An Artificial Surface Preconstruction. *Adv. Energy Mater.* **2020**, *10* (35), 2001120.

(32) Zhao, Y.; Liu, J.; Wang, S.; Ji, R.; Xia, Q.; Ding, Z.; Wei, W.; Liu, Y.; Wang, P.; Ivey, D. G. Surface Structural Transition Induced by Gradient Polyanion-Doping in Li-Rich Layered Oxides: Implications for Enhanced Electrochemical Performance. *Adv. Funct. Mater.* **2016**, *26* (26), 4760–4767.

(33) Luo, D.; Ding, X.; Fan, J.; Zhang, Z.; Liu, P.; Yang, X.; Guo, J.; Sun, S.; Lin, Z. Accurate Control of Initial Coulombic Efficiency for Lithium-rich Manganese-based Layered Oxides by Surface Multi-component Integration. *Angew. Chem., Int. Ed.* **2020**, *59* (51), 23061–23066.

(34) Li, B.; Yan, H.; Ma, J.; Yu, P.; Xia, D.; Huang, W.; Chu, W.; Wu, Z. Manipulating the Electronic Structure of Li-Rich Manganese-Based Oxide Using Polyanions: Towards Better Electrochemical Performance. *Adv. Funct. Mater.* **2014**, *24* (32), 5112–5118.

(35) Jiang, Y.; Yu, F.; Que, L.; Deng, L.; Xia, Y.; Ke, W.; Han, Y.; Wang, Z. Revealing the Thermodynamics and Kinetics of In-Plane Disordered  $\text{Li}_2\text{MnO}_3$  Structure in Li-Rich Cathodes. *ACS Energy Lett.* **2021**, *6* (11), 3836–3843.

(36) Song, J.; Li, B.; Chen, Y.; Zuo, Y.; Ning, F.; Shang, H.; Feng, G.; Liu, N.; Shen, C.; Ai, X.; Xia, D. A High-Performance Li-Mn-O Li-rich Cathode Material with Rhombohedral Symmetry via Intralayer Li/Mn Disorder. *Adv. Mater.* **2020**, *32* (16), No. e2000190.

(37) Wu, T.; Liu, X.; Zhang, X.; Lu, Y.; Wang, B.; Deng, Q.; Yang, Y.; Wang, E.; Lyu, Z.; Li, Y.; Wang, Y.; Lyu, Y.; He, C.; Ren, Y.; Xu, G.; Sun, X.; Amine, K.; Yu, H. Full Concentration Gradient-Tailored Li-Rich Layered Oxides for High-Energy Lithium-Ion Batteries. *Adv. Mater.* **2021**, *33* (2), 2001358.

(38) Nayak, P. K.; Erickson, E. M.; Schipper, F.; Penki, T. R.; Munichandraiah, N.; Adelhelm, P.; Sclar, H.; Amalraj, F.; Markovsky,

B.; Aurbach, D. Review on Challenges and Recent Advances in the Electrochemical Performance of High Capacity Li- and Mn-Rich Cathode Materials for Li-Ion Batteries. *Adv. Energy Mater.* **2018**, *8* (8), 1702397.

(39) Zhang, Y.; Chen, Z.; Shi, X.; Meng, C.; Das, P.; Zheng, S.; Pan, F.; Wu, Z. Regulation of 3d-Transition Metal Interlayered Disorder by Appropriate Lithium Depletion for Li-Rich Layered Oxide with Remarkably Enhanced Initial Coulombic Efficiency and Stability. *Adv. Energy Mater.* **2023**, *13* (5), 2203045.

(40) Ito, A.; Li, D.; Sato, Y.; Arao, M.; Watanabe, M.; Hatano, M.; Horie, H.; Ohsawa, Y. Cyclic deterioration and its improvement for Li-rich layered cathode material  $\text{Li}[\text{Ni}_{0.17}\text{Li}_{0.2}\text{Co}_{0.07}\text{Mn}_{0.56}]\text{O}_2$ . *J. Power Sources* **2010**, *195* (1), 567–573.

(41) van Bommel, A.; Krause, L.; Dahn, J. Investigation of the Irreversible Capacity Loss in the Lithium-Rich Oxide  $\text{Li}[\text{Li}_{1/3}\text{Ni}_{1/3}\text{Mn}_{3/3}]\text{O}_2$ . *J. Electrochem. Soc.* **2021**, *158* (6), 731–735.

(42) Yang, Z.; Zhong, J.; Feng, J.; Li, J.; Kang, F. Highly Reversible Anion Redox of Manganese-Based Cathode Material Realized by Electrochemical Ion Exchange for Lithium-Ion Batteries. *Adv. Funct. Mater.* **2021**, *31* (48), 2103594.

(43) Xu, J.; Sun, M.; Qiao, R.; Renfrew, S. E.; Ma, L.; Wu, T.; Hwang, S.; Nordlund, D.; Su, D.; Amine, K.; Lu, J.; McCloskey, B.; Yang, W.; Tong, W. Elucidating anionic oxygen activity in lithium-rich layered oxides. *Nat. Commun.* **2018**, *9* (1), 947.

(44) Shen, S.; Hong, Y.; Zhu, F.; Cao, Z.; Li, Y.; Ke, F.; Fan, J.; Zhou, L.; Wu, L.; Dai, P.; Cai, M.; Huang, L.; Zhou, Z.; Li, J.; Wu, Q.; Sun, S. Tuning Electrochemical Properties of Li-Rich Layered Oxide Cathodes by Adjusting Co/Ni Ratios and Mechanism Investigation Using in situ X-ray Diffraction and Online Continuous Flow Differential Electrochemical Mass Spectrometry. *ACS Appl. Mater. Interfaces* **2018**, *10* (15), 12666–12677.

(45) House, R. A.; Marie, J.-J.; Pérez-Osorio, M. A.; Rees, G. J.; Boivin, E.; Bruce, P. G. The role of  $\text{O}_2$  in O-redox cathodes for Li-ion batteries. *Nat. Energy* **2021**, *6* (8), 781–789.

(46) Armstrong, A. R.; Holzapfel, M.; Novak, P.; Johnson, C. S.; Kang, S.-H.; Thackeray, M. M.; Bruce, P. G. Demonstrating Oxygen Loss and Associated Structural Reorganization in the Lithium Battery Cathode  $\text{Li}[\text{Ni}_{0.2}\text{Li}_{0.2}\text{Mn}_{0.6}]\text{O}_2$ . *J. Am. Chem. Soc.* **2006**, *128* (26), 8694–8698.

(47) Tran, N.; Croguennec, L.; Menetrier, M.; Weill, F.; Biensan, P.; Jordy, C.; Delmas, C. Mechanisms Associated with the “Plateau” Observed at High Voltage for the Overlithiated  $\text{Li}_{1.12}(\text{Ni}_{0.425}\text{Mn}_{0.425}\text{Co}_{0.15})_{0.88}\text{O}_2$  System. *Chem. Mater.* **2008**, *20* (15), 4815–4825.

(48) Armstrong, A. R.; Holzapfel, M.; Novak, P.; Johnson, C. S.; Kang, S.-H.; Thackeray, M. M.; Bruce, P. G. Demonstrating Oxygen Loss and Associated Structural Reorganization in the Lithium Battery Cathode  $\text{Li}[\text{Ni}_{0.2}\text{Li}_{0.2}\text{Mn}_{0.6}]\text{O}_2$ . *J. Am. Chem. Soc.* **2006**, *128* (26), 8694–8698.

(49) Jiang, Y.; Yu, F.; Que, L.; Deng, L.; Xia, Y.; Ke, W.; Han, Y.; Wang, Z. Revealing the Thermodynamics and Kinetics of In-Plane Disordered  $\text{Li}_2\text{MnO}_3$  Structure in Li-Rich Cathodes. *ACS Energy Lett.* **2021**, *6* (11), 3836–3843.

(50) Sathiyaraj, M.; Abakumov, A. M.; Foix, D.; Rousse, G.; Ramesha, K.; Saubanère, M.; Doublet, M. L.; Vezin, H.; Laisa, C. P.; Prakash, A. S.; Gonbeau, D.; VanTendeloo, G.; Tarascon, J. Origin of voltage decay in high-capacity layered oxide electrodes. *Nat. Mater.* **2015**, *14* (2), 230–238.

(51) Gent, W. E.; Lim, K.; Liang, Y.; Li, Q.; Barnes, T.; Ahn, S.; Stone, K. H.; McIntire, M.; Hong, J.; Song, J. H.; et al. Coupling between oxygen redox and cation migration explains unusual electrochemistry in lithium-rich layered oxides. *Nat. Commun.* **2017**, *8* (1), 2091.

(52) Liu, W.; Oh, P.; Liu, X.; Lee, M. J.; Cho, W.; Chae, S.; Kim, Y.; Cho, J. Nickel-Rich Layered Lithium Transitional-Metal Oxide for High-Energy Lithium-Ion Batteries. *Angew. Chem., Int. Ed.* **2015**, *54* (15), 4440–4458.

(53) Ohzuku, T.; Ueda, A.; Nagayama, M. Electrochemistry and Structural Chemistry of  $\text{LiNiO}_2$  (R-3m) for 4 V Secondary Lithium Cells. *J. Electrochem. Soc.* **1993**, *140* (7), 1862–1870.

(54) McCalla, E.; Abakumov, A. M.; Saubanere, M.; Foix, D.; Berg, E. J.; Rousse, G.; Doublet, M.-L.; Gonbeau, D.; Novak, P.; Van Tendeloo, G.; Dominko, R.; Tarascon, J.-M. Visualization of O-O peroxo-like dimers in high-capacity layered oxides for Li-ion batteries. *Science* **2015**, *350* (6267), 1516–1521.

(55) Jansen, M.; Nuss, H. Ionic Ozonides. *Z. Anorg. Allg. Chem.* **2007**, *633* (9), 1307–1315.